Spontaneous Generation of Low-Frequency Modes of Variability in the Wind-Driven Ocean Circulation

ERIC SIMONNET AND HENK A. DIJKSTRA

Institute for Marine and Atmospheric Research Utrecht, Department of Physics and Astronomy, Utrecht University, Utrecht, Netherlands

ABSTRACT

In idealized models that aim to understand the temporal variability of the wind-driven ocean circulation, low-frequency instabilities associated with so-called oscillatory gyre modes have been found. For the double-gyre case, the spectral origin of these modes as well as the physical mechanism of the instability is explained. In a barotropic quasigeostrophic model, the low-frequency modes arise spontaneously from the merging between two nonoscillatory eigenmodes. Of the latter two, one is called here the P-mode and is responsible for the existence of multiple steady states. The other is called the L-mode and it controls the intensity of the gyres. This merging turns out to be robust over a hierarchy of models and can even be found in a low-order truncated quasigeostrophic model. The latter model is used to determine the physical mechanism of the instability. The low-frequency oscillation results from the conjugate effects of shear- and symmetry-breaking instabilities and is free of Rossby wave dynamics.

1. Introduction

Over the last decade, much work has been dedicated to determining the physics of low-frequency (interannual and longer timescale) variability in the midlatitude wind-driven ocean circulation. Modeling studies of the wind-driven ocean gyres have shown that intrinsic variability on a wide range of timescales, from seasonal up to interdecadal, exists (Jiang et al. 1995; McCalpin and Haidvogel 1996; Spall 1996; Berloff and McWilliams 1999; Meacham 2000). Time-dependent fluctuations of external wind forcing are not needed to generate this low-frequency behavior. It arises spontaneously through nonlinear processes within the subtropical and subpolar gyres and the midlatitude jet system.

Many steps are necessary to fully understand the observed large-scale and low-frequency fluctuations of the major western boundary currents, such as the Gulf Stream or Kuroshio. Fortunately, there is a rich and subtle hierarchy of models available to make progress toward this goal. At the low end of this hierarchy, there are single-layer barotropic quasigeostrophic (QG) (Cessi and Ierley 1995; Sheremet et al. 1997) as well as shallow-water models (Jiang et al. 1993, 1995; Speich et al. 1995). It has now become a classical problem in physical oceanography to study solutions of these nonlinear models.

These flows are usually forced by a steady idealized cosine wind stress shape leading to the appearance of only the subtropical gyre (called the "single-gyre case") or both the subtropical and subpolar gyre (the "double-gyre" case). Multilayer models with an idealized geometry represent the next step to understand the behavior of fully three-dimensional ocean models. Baroclinic physics indeed appears to play a role in low-frequency variability (Dijkstra and Katsman 1997; Berloff and McWilliams 1999; Ghil et al. 2002, hereafter GFS; Nauw and Dijkstra 2001; Simonnet et al. 2001a, submitted to *J. Phys. Oceanogr.*; Simonnet et al. 2001b, submitted to *J. Phys. Oceanogr.*, hereafter SGITW). The effect of asymmetric wind stress profiles (McCalpin and Haidvogel 1996; Berloff and McWilliams 1999) and continental geometry and/or bathymetry (Dijkstra and Molemaker 1999; Schmeits and Dijkstra 2000; SGITW; Nauw and Dijkstra 2001) has also gained attention.

When the time-dependent solutions of these models are considered in a highly nonlinear regime, one easily finds low-frequency variability. However, to pin down the responsible dynamical mechanisms is difficult. Studies on the route to complex behavior of these flows through successive bifurcations have indicated several dynamical possibilities. A first possibility is that (unstable) steady states may steer the temporal behavior of the solutions along the high-dimensional stable manifolds (Cessi and Ierley 1995; Primeau 2001). A second one is that in highly nonlinear regimes, low-frequency variability arises naturally due to the appearance of

---

Corresponding author address: Dr. Eric Simonnet, Department of Atmospheric Sciences, Institute of Geophysics and Planetary Physics, University of California, Los Angeles, Los Angeles, CA 90095-1565.
E-mail: simonnet@atmos.ucla.edu

homoclinic and/or heteroclinic orbits (Berloff and McWilliams 1999; Meacham 2000; Chang et al. 2001; SGITW).

The appearance of global bifurcations in the form of homoclinic orbits is more likely to be expected in the case where multiple steady states coexist (Chang et al. 2001). Such dynamical behavior suggests the existence of multiple oceanic states that bear a noticeable resemblance with the atmosphere, where they are referred to as weather regimes (e.g., Mo and Ghil 1988; Corti et al. 1999; Plaut and Simonnet 2001). There are indications for the dynamical existence of these multiple steady states, for instance, in the Kuroshio and Gulf Stream currents (Schmeits and Dijkstra 2001). However, in such highly nonlinear regimes, it is often difficult to clarify the link between the low-frequency variability due to regime switches and the low-frequency modes of variability arising at the early Hopf bifurcations. A third possibility is therefore that the first limit cycles tend to leave their spectral imprints on highly chaotic motions (Nauw and Dijkstra 2001).

Hence, it may be quite wrong to underestimate the role of the first oscillatory modes that become unstable when forcing (friction) is increased (decreased). For the double-gyre circulation, these modes are of several types. The first type is high-frequency Rossby basin modes, which are forced, dissipative modifications of the inviscid basin modes (Pedlosky 1987). The second type is classical baroclinic instabilities, that are found in multilayer models in cases where the internal Rossby radius of deformation is small (Dijkstra and Katsman 1997; GFS; SGITW). A third type is wall-trapped modes that correspond to localized instabilities confined to the region of the western boundary current (Ierley and Young 1991; Chang et al. 2001). The fourth type of modes is referred to as (oscillatory) gyre modes; in many respects, these modes are less well understood.

Although the spatial pattern of such a gyre mode is wavelike, the mode does not originate from the spectrum of a linear operator related to free wave propagation. It has been called an oscillatory gyre mode because it simply disappears when the intensity of the gyres becomes too weak (Dijkstra and Katsman 1997). Its direction of propagation does not appear to be related to that of the Rossby waves but it propagates perpendicularly to the direction of the midlatitude jet, which makes the jet fluctuate in intensity. Its appearance is thus deeply linked to the existence of fully developed recirculation gyres. It also distinguishes itself from the other instabilities by its much longer oscillation period, which is interannual (decadal) in a barotropic (baroclinic) model. Finally, it is one of the most robust features of the wind-driven double-gyre circulation. It can be found in Fig. 8 of Jiang et al. (1995), Fig. 9 of Speich et al. (1995), Fig. 6 of Dijkstra and Katsman (1997), Fig. 6 of Dijkstra and Molemaker (1999), Fig. 15 of Berloff and McWilliams (1999), Fig. 11 of Chang et al. (2001), Fig. 2 of SGITW, and Fig. 6 of Nauw and Dijk-

stra (2001). In fact, we are not aware of idealized models of the double-gyre circulation where it is missing.

The purpose of this paper is to understand the spectral origin of this low-frequency gyre mode and to describe the physical mechanisms of its growth and propagation. Although the mode occurs in many models, we consider it here in one of the simplest models of the double-gyre circulation, that is, a barotropic single-layer QG model (section 2). We show that the *gyre mode* originates from the merging of two nonoscillatory modes. One of these modes, which we call the P-mode, is associated with the occurrence of multiple equilibria. The other mode, which we call L-mode, controls the (energy) intensity of the whole double-gyre flow. These two eigenmodes are merging smoothly once the steady-state solution becomes sufficiently asymmetric to generate "spontaneously" the low-frequency oscillatory gyre mode (section 3). This merging also occurs in a severely truncated QG model due to Jiang et al. (1995). In section 4, the latter model is used to determine the physical oscillation mechanisms of the gyre mode. In the last section, the results are summarized and discussed.

2. Model and methods

One of the simplest models of the wind-driven ocean circulation is the classical barotropic QG model. It has been shown that this model, in either its barotropic or reduced-gravity version, provides rich insights into the nonlinear dynamics of the double-gyre circulation (McCalpin and Haidvogel 1996; Chang et al. 2001).

a. Model

We use here a barotropic single-layer version of the two-layer model of Dijkstra and Katsman (1997). The ocean layer has a constant density ρ and mean thickness D and is confined to a square basin of horizontal dimensions $L \times L$. The flow in the basin is forced by a wind stress $(\tau_0 \tau^x, \tau_0 \tau^y)$, where τ_0 is a characteristic amplitude. Both bottom friction (with coefficient ϵ_0) and lateral friction (with coefficient A_H) are considered. Using characteristic horizontal and vertical scales L and D, a horizontal velocity scale U, a wind stress scale τ_0, and a timescale L/U, the nondimensional equations become

$$\frac{\partial}{\partial t}(\nabla^2\psi - F\psi) + J(\psi, \nabla^2\psi - F\psi) + \beta\frac{\partial\psi}{\partial x}$$

$$= \text{Re}^{-1}\nabla^2\zeta - \mu\zeta + \alpha\left(\frac{\partial\tau^y}{\partial x} - \frac{\partial\tau^x}{\partial y}\right), \quad (1)$$

where J is the Jacobian defined as

$$J(a, b) = \frac{\partial a}{\partial x}\frac{\partial b}{\partial y} - \frac{\partial a}{\partial y}\frac{\partial b}{\partial x},$$

ψ is the geostrophic streamfunction, and ζ is the vertical

TABLE 1. Reference values of parameters in the barotropic QG model.

Parameter	Value	Parameter	Value
	Dimensional		
U	7.1×10^{-3} m s^{-1}	L	1.0×10^{6} m
L/U	4.46 yr	D	2500 m
τ_0	1.26×10^{-1} Pa	β_0	7.1×10^{-12} (m s)$^{-1}$
ρ	1×10^{3} kg m^{-3}	f_0	5.0×10^{-5} s^{-1}
	Dimensionless		
α	10^{3}	β	10^{3}
F	0	μ	0
δ_I	0.032	δ_M	(0.02 – 0.04)

component of the vorticity vector, that is, $\zeta = \nabla^2 \psi$. The parameters in (1) are the Reynolds number Re, the strength of the planetary vorticity gradient β, the strength of the wind stress α, the rotational Froude number F, and the bottom friction parameter μ. Their expressions are given as

$$\mathrm{Re} = \frac{UL}{A_H}; \qquad \alpha = \frac{\tau_0 L}{\rho D U^2}; \qquad \beta = \frac{\beta_0 L^2}{U};$$

$$\mathrm{F} = \frac{f_0^2 L^2}{gD}; \qquad \mu = \frac{L\epsilon_0}{U}. \qquad (2)$$

In the results of section 3 below, both μ and F are set to zero, and the Reynolds number Re is used as the control parameter. The reference values of the other parameters are indicated in Table 1. The values of the dimensionless inertial and viscous boundary layer thickness, $\delta_I = L^{-1}\sqrt{U/\beta_0}$ and $\delta_M = L^{-1}(A_H/\beta_0)^{1/3}$, are also indicated.

The flow in the basin is forced by an idealized zonal wind stress that is constant in time, given by

$$\tau^x = -\frac{1}{2\pi}(1 - \sigma)\cos 2\pi y + \frac{\sigma}{2\pi}\cos \pi y,$$

$$\tau^y = 0, \qquad (3)$$

where the "homotopy" parameter σ controls the shape of the wind stress. The case $\sigma = 0$ corresponds to an antisymmetric wind stress curl whereas for nonzero σ, the wind stress is asymmetric. The total vorticity input into the basin is thus nonzero for $\sigma \neq 0$. Depending on the sign of σ, the solution obtained has either a more intense subtropical ($\sigma < 0$) or subpolar gyre ($\sigma > 0$). In the case of $\sigma < 0$, the relative size of the subtropical gyre is smaller than the subpolar one.

Free-slip boundary conditions are imposed on the northern and southern walls ($y = 0, 1$) and no-slip boundary conditions on the eastern and western walls ($x = 0, 1$). A 64×64 nonequidistant grid is used with the same stretching parameters ($q_x = q_y = 2$) as in Dijkstra and Katsman (1997). With this resolution, the western boundary layers are nicely resolved, without the need to achieve high resolution in the interior part

of the basin, and the positions of the bifurcation points have converged.

b. Numerical methods

Numerical bifurcation tools are now widely used in the study of the wind-driven double-gyre flow (Speich et al. 1995; Dijkstra and Katsman 1997; Primeau 1998; Simonnet 1998). The basic idea is to compute directly a branch of steady-state solutions as one (physical) parameter is varied, instead of merely computing just one steady state, for a set of parameter values, by forward integration in time. These techniques are often referred to as continuation methods or pseudoarclength methods (Keller 1977) and have been introduced into geophysical fluid dynamics by Legras and Ghil (1985). Various descriptions and applications of these methods for systems of partial differential equations can be found in Kubiček and Marek (1983), in Doedel and Tuckerman (2000), and in Dijkstra (2000).

After discretization, the computation of a steady state amounts to solve a set of nonlinear algebraic equations in a large-dimensional space. These equations can be written as

$$\mathbf{F}[\mathbf{x}(s); \mathbf{p}(s)] = 0, \qquad (4)$$

where $\mathbf{x}$ is the discretized n-dimensional solution and $\mathbf{p}$ is the p-dimensional vector of parameters. Current computer hardware allows typical values of $n = O(10^4 - 10^5)$. The use of an additional parameter s, which approximates the arclength along the branch of solutions, enables one to go easily around saddle-node bifurcation points. The tangent to the branch of solutions is normalized, giving

$$\left(\frac{d\mathbf{x}_0}{ds}\right)^{\mathrm{T}}(\mathbf{x} - \mathbf{x}_0) + \frac{d\mu_0}{ds}(\mu - \mu_0) - \Delta s = 0, \quad (5)$$

where $(\mathbf{x}_0, \mu_0)$ corresponds to a known solution on the branch—that has been obtained analytically or been previously computed—and Δs is the chosen steplength. The system (4) and (5) is solved by a Newton–Raphson method.

As one follows a branch of steady-state solutions, transitions to multiple equilibria—via pitchfork or saddle-node bifurcations—or periodic behavior, via Hopf bifurcations, can be found by monitoring the linear stability of the steady states. Several studies have shown that only a very small number of (complex) eigenvalues are involved in the transition from multiple equilibria to irregular behavior in the double-gyre circulation (Dijkstra and Molemaker 1999; SGITW). This type of situation is often encountered in fluid dynamics and specific algorithms dedicated to the computation of the leading part of the spectrum have been developed. The discretized linear stability problem leads to a generalized eigenvalue problem of the form

$$A\mathbf{\Phi} = \kappa B\mathbf{\Phi}, \qquad \kappa = \kappa_r + i\kappa_i, \qquad (6)$$

with $A = \partial_x \mathbf{F}(\mathbf{x}_0; \mu_0)$. The matrix B, which arises from the time derivatives in (1), may be singular due to the boundary conditions or other constraints. The eigenfunction $\mathbf{\Phi}_r + i\mathbf{\Phi}_i$ and the complex pair of eigenvalues $\kappa_r + i\kappa_i$ provide the time periodic disturbance structure $\mathbf{\Phi}(t)$ with angular frequency κ_i and growth rate κ_r; that is,

$$\mathbf{\Phi}(t) = e^{\kappa_r t}[\mathbf{\Phi}_r \cos\kappa_i t - \mathbf{\Phi}_i \sin\kappa_i t]. \tag{7}$$

In order to compute the ''most dangerous'' eigenvalues, that is, the ones near the imaginary axis, we use the simultaneous iteration technique (SIT) of Stewart and Jennings (1981). A description of the SIT algorithm can also be found in Speich et al. (1995) and Dijkstra (2000).

3. Spectral origin of the oscillatory gyre mode

When forced by a purely antisymmetric wind stress curl, Eq. (1) have a mirror symmetry R with respect to the midaxis of the basin, which can be represented by

$$R[\psi(x, y)] = -\psi(x, 1 - y). \tag{8}$$

If the operator E represents Eq. (1) with the appropriate boundary conditions, then it is easy to show that for every solution ψ,

$$(R \circ E)\psi = (E \circ R)\psi. \tag{9}$$

Steady solutions ψ of (1) always come in mirror pairs because if ψ is a solution, then $R\psi$ is a steady solution as well. This property has a strong impact on the bifurcation structure of (1) since symmetry-breaking pitchfork bifurcations are, in this case, generic (Golubitsky and Schaeffer 1985).

a. Branching structure and instabilities

The impact of the symmetry property (9) is readily observable in Fig. 1, where the basic bifurcation diagram together with the steady streamfunction patterns are shown for the case $\sigma = 0$, F $= 0$, and $\mu = 0$.

The vertical axis in Fig. 1 corresponds to the non-dimensional intensity of the subtropical gyre, that is, $\psi_{\text{subtropical}} = \max_{\psi>0} \psi$, while the Reynolds number Re is shown on the horizontal axis. We obtain three distinct branches of solutions similar to those found by Cessi and Ierley (1995) and Dijkstra and Katsman (1997). The first branch is characterized by perfectly antisymmetric solutions ψ for which $R\psi = \psi$. After the first saddle-node bifurcation point L (see Fig. 1), these solutions become inertially dominated, the flows become very energetic, and the recirculation gyres eventually fill the entire basin. Two pitchfork bifurcations P_1 and P_2 occur on the antisymmetric branch at Re $= 29.4$ and Re $= 39.3$, respectively. They are responsible for the appearance of asymmetric solutions, which come in mirror pairs due to (9). The second pitchfork bifurcation at P_2 leads to a branch of asymmetric flows with their jet aligned in the west–east direction and a confluence point

either shifted to the south or to the north of the midaxis of the basin (see Fig. 1, upper-right panel).

We will not consider the latter solutions in more detail, but focus instead on the two branches of asymmetric solutions that start at P_1 and form a mirror pair for each Re value. The flows on both branches exhibit meandering of the jet downstream of the recirculation dipole (see details in Chang et al. 2001), with either a stronger subtropical gyre (upper branch) or a stronger subpolar gyre (lower branch). The weaker gyre is more affected by the asymmetry and wraps around the stronger one. We call therefore the upper and lower asymmetric branches merging at P, the ''jet-south'' and the ''jet-north'' branch, respectively.

The dependence on Re of the real (left panel) and imaginary (right panel) part of the leading eigenvalues κ along these two branches is shown in Fig. 2. The solutions on either asymmetric branch are linearly stable up to the first Hopf bifurcation H_1, at Re $= 71.5$. The first oscillatory mode that becomes unstable is a Rossby basin mode with an oscillation period of 7 months. At the second Hopf bifurcation H_{gyre} (at Re $= 83.2$), a gyre mode with an oscillation period of 1.8 yr becomes unstable. At the third Hopf bifurcation H_3, a second gyre mode, with an oscillation period of 2.2 yr, destabilizes. These results are qualitatively similar to those found in Dijkstra and Katsman (1997), where only the first two Hopf bifurcations were determined. The oscillatory gyre modes are characterized by a southwestward (north-westward) propagation of the anomalies in the case where the subtropical (subpolar) gyre is more intense.

b. Mode merging

As can be seen in Fig. 2, the oscillatory gyre mode that becomes unstable at H_{gyre} has a negative growth factor for smaller Re. In the right panels of Fig. 3a, the pattern of the real and imaginary parts of this mode is shown near Re $= 40$. In order to understand the origin of this mode, the eigensolution is ''traced back'' smoothly to smaller Re. At each step, we carefully check that the behavior of the eigensolution, with the characteristics of the oscillatory gyre mode, changes continuously, so that no ambiguity is possible. In the context of QG dynamics, this is made easier due to the large spectral separation between the different Hopf bifurcations, which prevails in the double-gyre problem (Dijkstra and Molemaker 1999). The path of the gyre mode (the dash-dotted curve in Fig. 3) ends at the point M, where it splits into two stationary modes. These two modes exist up to the point P_1 where the asymmetric solutions disappear for lower values of Re.

Also shown in Fig. 3a are the leading eigenmodes on the antisymmetric solution branch. The nonoscillatory mode responsible for both the first and the second pitchfork bifurcation (P_1 and P_2) has a symmetric tripolar structure (upper-left panel). At P_1, the growth rate κ_r of this mode becomes positive, which means that the an-
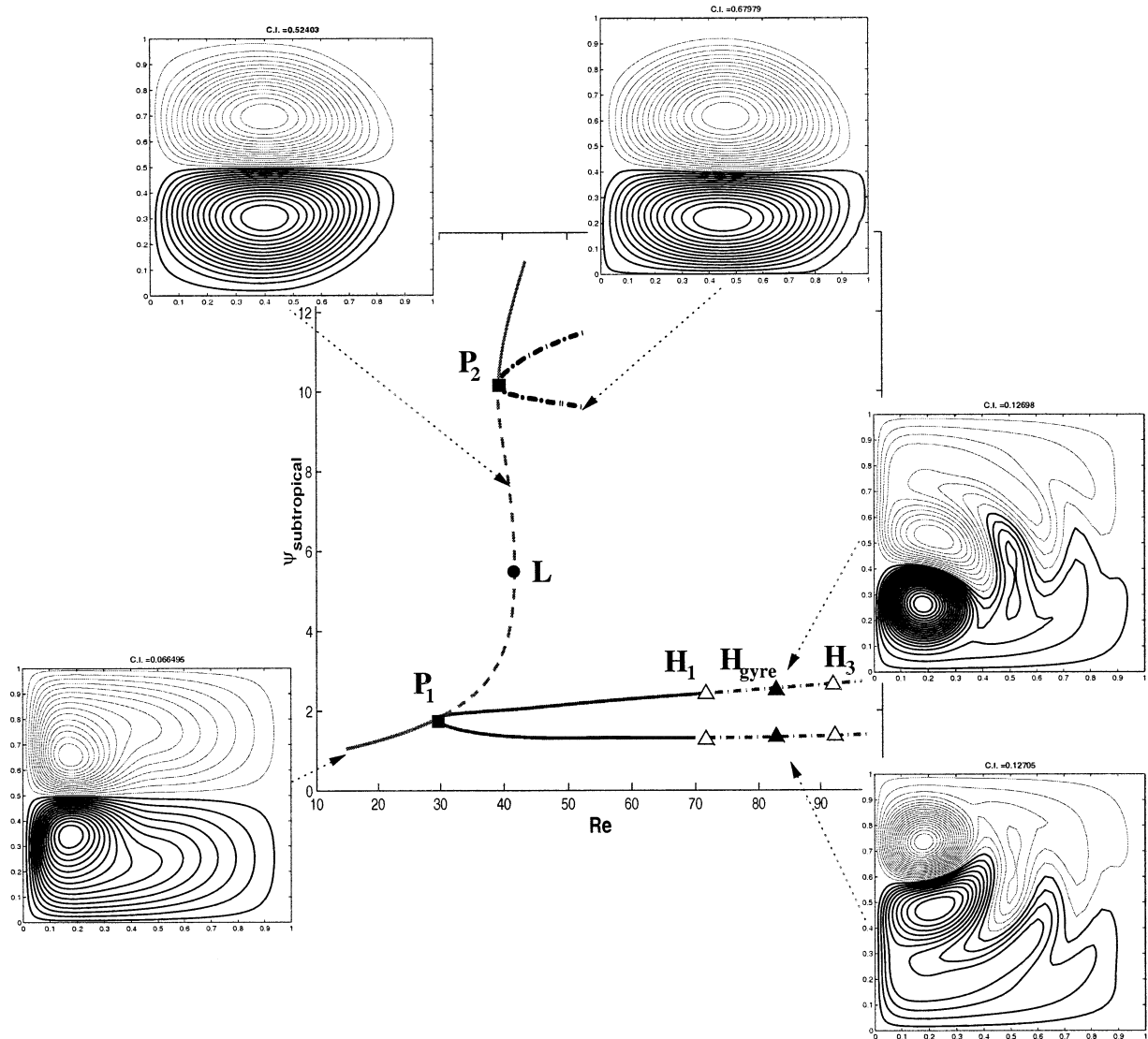
FIG. 1. Bifurcation diagram for the QG model with values of the parameters as in Table 1. Here Ψ subtropical vs the Reynold number Re is plotted together with the flow patterns. The bifurcations P_1, P_2 correspond to the pitchfork bifurcations (squares), whereas the triangles indicate the location of the Hopf bifurcations (see text and Fig. 2 for details), the first limit point L is indicated by a dot. The panels correspond to the upper-layer streamfunctions, positive contours are represented by thick lines, negative contours by thin lines together with contour intervals.

tisymmetric steady flow becomes unstable to this perturbation pattern. Basically, the superposition of such a symmetric perturbation on the antisymmetric steady state creates either a stronger subpolar gyre or a stronger subtropical one. When Re > 29.4, the perturbation is able to extract enough energy from the horizontal shear of the basic state so as to overcome the effect of the dissipation (Dijkstra and Katsman 1997; Primeau 1998). Because this mode is responsible for multiple equilibria and asymmetric states under symmetric forcing conditions, that is, for the pitchfork bifurcations, we call it the P-mode. The P-mode streamfunction keeps its symmetric structure unchanged over the whole Re range explored herein.

The nonoscillatory mode responsible for the saddle–node bifurcation at L and the one just before P_2 has a dipolar antisymmetric structure (Fig. 3a, lower-left panel). It thus acts on both gyres simultaneously so that they either increase or decrease in intensity. The antisymmetric structure of the steady flow is thus kept unchanged due to the equally antisymmetric structure of the perturbation. We will call this nonoscillatory mode involved in the saddle–node bifurcations, or limit points, the L-mode. At P_1, the L-mode is stable with a growth rate $\kappa_r \approx -5$ and κ_r becomes positive at the saddle–node bifurcation L in Fig. 3a. When the L-mode perturbation has the sign shown, it increases the energy of both gyres. On the contrary, if the perturbation has the
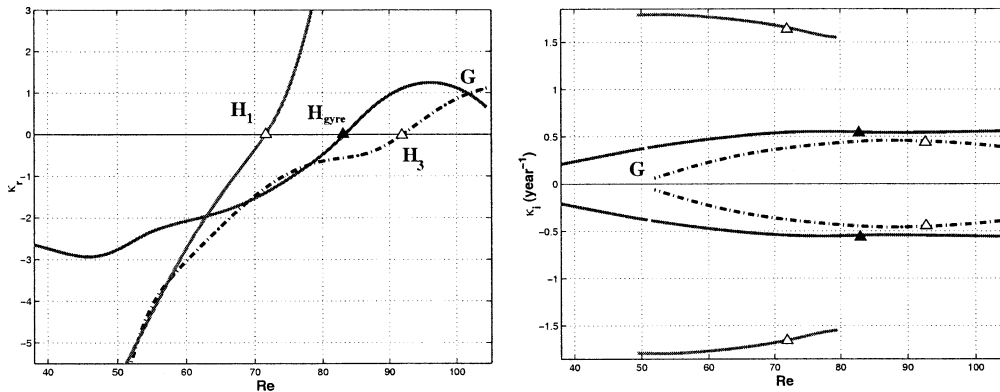
FIG. 2. Path of the three most dangerous eigenvalues for the QG model as a function of Re. The left panel corresponds to real parts and the right panel to the complex conjugate imaginary parts. The letter **G** refers to two distinct gyre modes in the QG model (see text). The triangles indicate the locations of the Hopf bifurcations.

opposite sign, both gyres will decrease simultaneously in intensity and the basic flow will become less energetic.

Relevant for the oscillatory gyre mode is the path of both the P-mode and L-mode along the two asymmetric branches for Re > 29.4. For Re slightly above P_1, both modes are still nonoscillatory and have a negative growth factor since both asymmetric branches are stable. The path of the eigenvalues of both modes is indicated by the heavy lines in Fig. 3 (starting at P_1). The growth factor of the P-mode decreases with Re, whereas that of the L-mode increases. Both modes meet at the point M (Fig. 3), which we call the *merging point,* and connect to the oscillatory gyre mode. Figure 3b shows the three-dimensional evolution of the eigenvalues in the complex plane as a function of Re. Two parabolic curves are tangent at M; one parabola is located in the plane $\kappa_i = 0$ (the path of both P- and L-mode) whereas the other (the gyre mode) is located in a plane of (nearly) constant negative κ_r.

In Fig. 4, the variations of the streamfunction pattern of the P-mode and L-mode along the asymmetric branch of "jet-south" solutions (from P_1 to M) in Fig. 3 are plotted. The tripole shaped P-mode is deformed by the asymmetry of the steady flow so that it becomes aligned with the direction of the jet and its structure becomes almost dipolar. The L-mode is not very much affected by the flow and keeps its pronounced dipolar shape. At M, these two modes are identical and merge to become complex conjugate. After the merging, the real part of the gyre mode pattern is inherited from the P-mode and becomes more asymmetric whereas the pattern of its imaginary part is similar to that of the L-mode. This demonstrates that the oscillatory gyre mode results from the merging of the P-mode and L-mode on either asymmetric branch of solutions.

c. Imperfections: Asymmetric wind stress

When the wind stress forcing is taken slightly asymmetric, that is, $\sigma \neq 0$ in (3), the internal QG reflection symmetry is broken. One then expects perturbed pitchfork bifurcations to lead to the appearance of disconnected branches of solutions, as is the case for the shallow-water models in the presence of symmetric wind stress (Jiang et al. 1995; Speich et al. 1995). The bifurcation diagram for $\sigma = 0.01$ (Fig. 5a) shows the disconnected branches that were connected at P_1 in the symmetric case; those disconnected from P_2 are not shown. A blowup of the vicinity of P is shown in Fig. 5b. Of the branches shown in the blowup, the one containing M_1 is referred to here as the "connected" branch and can be followed toward the linear Munk–Sverdrup flows at small Re (not shown). The other branch, which contains M_2, is referred to as the "isolated" branch and is characterized by stable and unstable steady solutions that are separated by a saddle–node bifurcation at L (Fig. 5b).

On each of the two branches, an oscillatory gyre mode appears: the one on the isolated branch is a "jet-north" mode while the one on the connected branch corresponds to a "jet-south" mode. The real part κ_r of this leading eigenmode of the linear stability problem is plotted in Fig. 5c along both branches. Merging of stationary modes (along the arrows in Fig. 5c) occurs on both branches and leads to the two distinct "gyre" modes. Indeed, the point M in Fig. 3 has now split into two different merging points, M_1 and M_2, which correspond to the appearance of the two (nearly) mirror-symmetric gyre modes. One can clearly imagine how restoring the broken symmetry ($\sigma \rightarrow 0$) acts on the branches of eigenvalues to give the picture of Fig. 3.

Shallow-water models are characterized by the appearance of perturbed pitchfork bifurcations even in the presence of symmetric forcing, because of their natural lack of symmetry due to thermocline deviations (Jiang et al. 1995; Dijkstra and Molemaker 1999). Their solution branches are therefore always disconnected, like those in Fig. 5. The results above explain why in situations of broken symmetry, including those of shallow-water models forced by a symmetric double-gyre wind
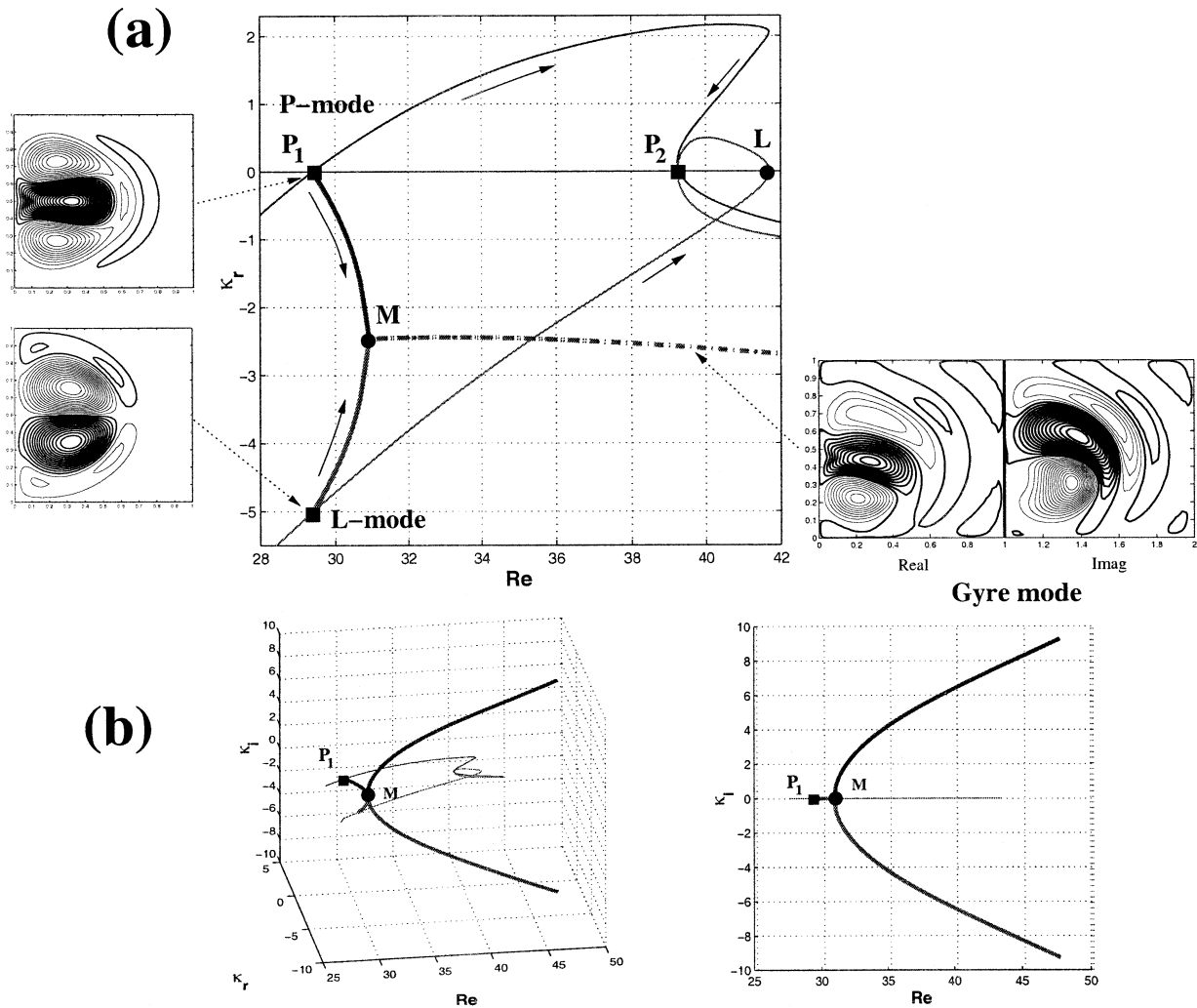
FIG. 3. Spectral behavior of the eigenmodes involved into the various bifurcations off the antisymmetric "jet-south" branch for the barotropic QG model (see Fig. 1). (a) The real part and (b) imaginary part of the P-mode and L-mode eigenvalues are plotted vs Re. Thick lines, beginning at P_1 and ending at M, correspond to the path of these two modes on the asymmetric branch, thin lines to the path on the antisymmetric branch. The dash–dot thick line indicates a nonzero imaginary part. At M, the merging between the P-mode and L-mode occurs. The various panels show the streamfunction patterns at the locations indicated by the arrows.

stress, oscillatory gyre modes are still found. We have therefore identified a robust feature of the double-gyre wind-driven ocean circulation, which is closely related to the existence of the P-mode and L-mode. This motivates us to look for even simpler models in which these modes appear and use them to gain further physical insight.

4. Physics of the oscillatory "gyre" mode

It turns out that the merging process occurs already in the low-order model of the wind-driven ocean circulation that was also studied by Jiang et al. (1995). Their model, following Veronis (1963), is based on the projection of the barotropic QG model on only two basis functions.

a. Low-order model

The low-order model derived by Jiang et al. (1995) starts from a dimensional version of Eq. (1) with zero lateral mixing ($A_H \rightarrow 0$), while keeping nonzero bottom friction ($\epsilon_0 \neq 0$). When we scale time, length, wind stress, and streamfunction by $1/(\beta_0 L)$, L, τ_0, and $\tau_0/(\rho\beta_0 D)$, respectively, their dimensionless QG model becomes

$$\frac{\partial}{\partial t}(\nabla^2 - F)\Psi + \epsilon J[\Psi, (\nabla^2 - F)\Psi] + \beta\frac{\partial\Psi}{\partial x}$$

$$= -\mu\nabla^2\Psi + w_f. \tag{10}$$

Here the parameters are slightly different than in section 2, with the Rossby number ϵ and μ now given by

29.41   **29.60**   **29.72**   **29.86**

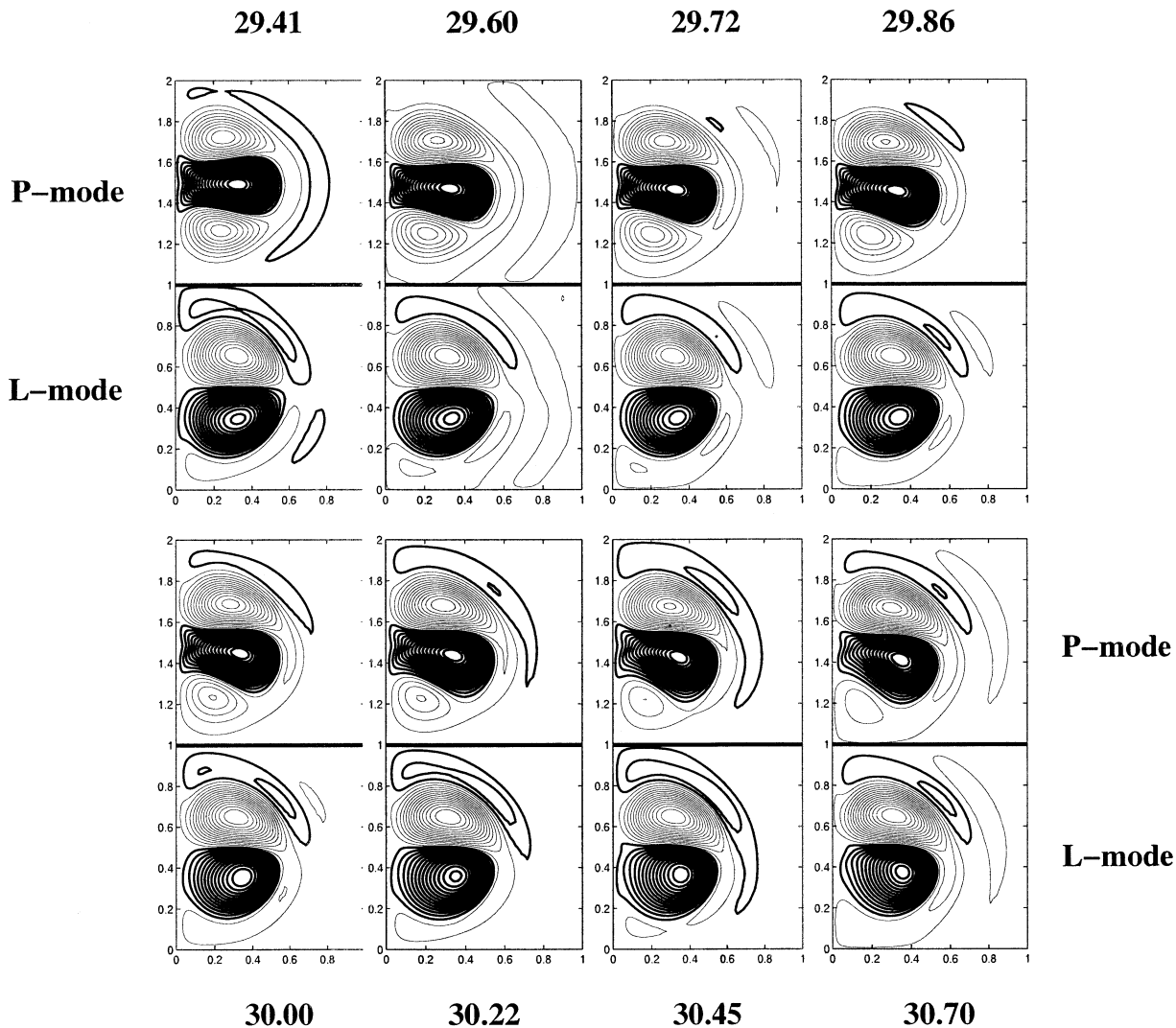**30.00**   **30.22**   **30.45**   **30.70**

FIG. 4. Merging of the P-mode and L-mode streamfunctions on the asymmetric branch as a function of Re from the pitchfork bifurcation P_1 at Re = 29.40 to the merging point M at Re = 30.90 (see thick line, Fig. 3).

$$\epsilon = \frac{\tau^0}{\rho D \beta_0^2 L^3}, \qquad \mu = \frac{\epsilon_0}{\beta_0 L}, \tag{11}$$

$$w_f = -\frac{\partial \tau^x}{\partial y}. \tag{12}$$

We consider now a square domain $(x, y) \in [0, \pi] \times [0, \pi]$, while on the boundaries the Eq. (10) accommodate only conditions of no-normal flow, that is, $\Psi = 0$.

The idea explored by Jiang et al. (1995) was to consider an expansion that is better adapted to the problem than the double Fourier series expansion of (10) in the x and y directions (Veronis 1963). In order to account for the existence of the western boundary layer, a decaying exponential in the x direction is introduced while a sine expansion is retained in the y direction; that is,

$$\Psi = A(t)G(x) \sin y + B(t)G(x) \sin 2y,$$

$$w_f = -w_1 \sin y - w_2 \sin 2y. \tag{13}$$

Here $s = 1.3$ is chosen such that $G(x) = e^{-sx} \sin x$ fits the zonally asymmetric structure of a typical double-gyre flow, while w_1 and w_2 correspond to the parameters that control the intensity of the antisymmetric and (a)symmetric part of the wind stress forcing, respectively.

The truncated equations are obtained by projecting (10) onto the orthogonal basis $\{G(x) \sin y, \ G(x) \sin 2y\}$. The variational expression uses the standard Hilbert product $\langle f, g \rangle = \int_0^\pi \int_0^\pi fg \, dx \, dy$. In this case, the energy of the truncated system is conserved. A system of two nonlinear differential equations for A and B is obtained as

$$\frac{dA}{dt} - \lambda AB + \nu_1 A = \eta_1$$

$$\frac{dB}{dt} + \lambda A^2 + \nu_2 B = \eta_2, \tag{14}$$
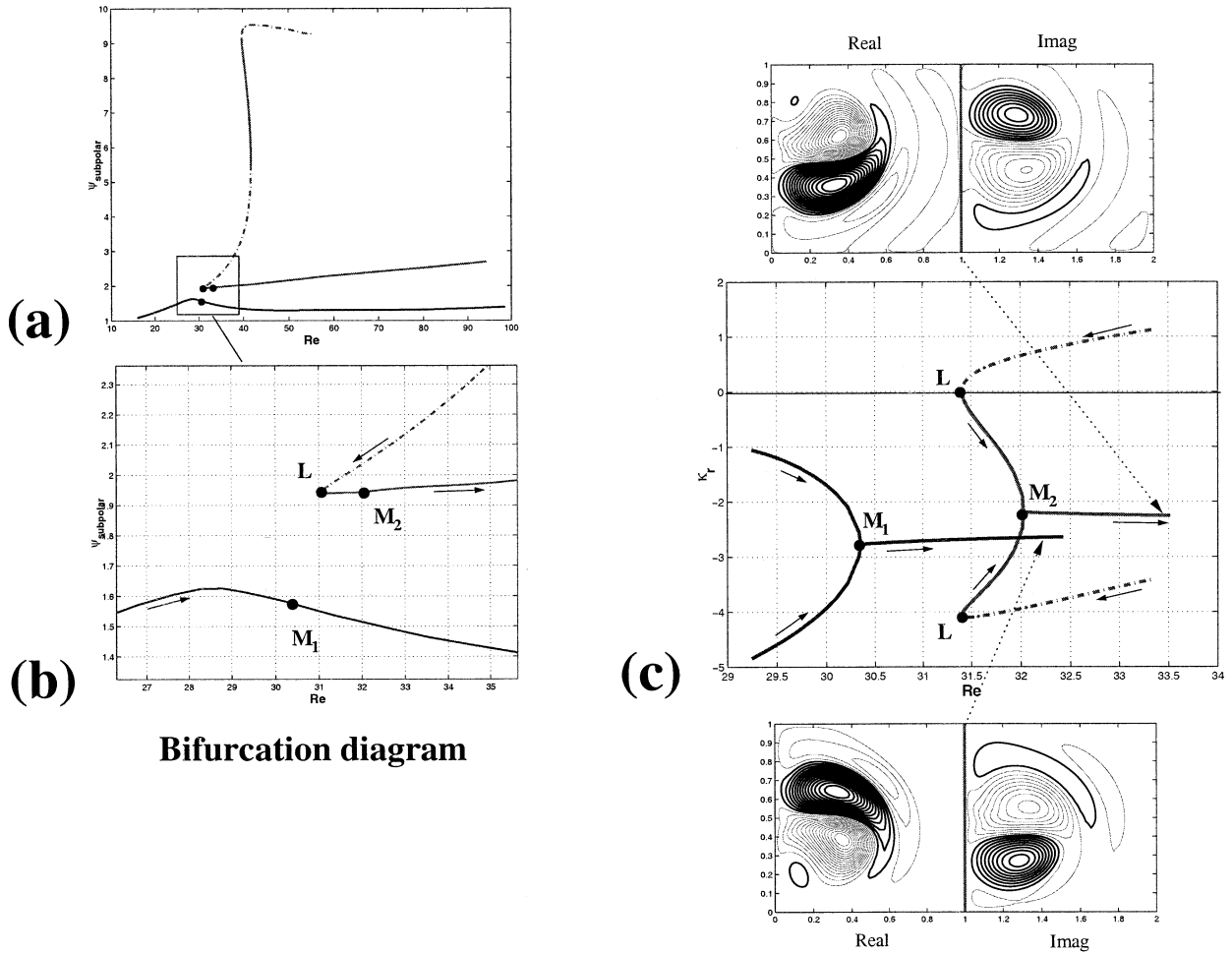
where

(a)

(b)

Bifurcation diagram

(c)

FIG. 5. (a) The bifurcation diagram (Ψ_{subpolar} vs Re) of the perturbed QG model. (b) A zoom of the region where the two merging processes occur. (c) Corresponds to the spectral behavior of the pair of mirror-symmetric gyre modes in the perturbed barotropic QG model, for the connected branch (left) and the disconnected one (right). The panels (up and down) correspond to the streamfunction eigenmodes; M_1 and M_2 represent the two points of merging.

$$\lambda = \epsilon \left(\frac{4s^2}{1 + 9s^2} \frac{s^2 + 1}{s^2 + 2 + F} \frac{1 + e^{-3s\pi}}{1 - e^{-2s\pi}} \right),$$

$$\nu_1 = \mu \left(\frac{s^2 + 2}{s^2 + 2 + F} \right), \qquad \nu_2 = \mu \left(\frac{s^2 + 5}{s^2 + 5 + F} \right), \quad (15)$$

$$\eta_1 = w_1 \left(\frac{4s}{s^2 + 2 + F} \frac{1}{1 - e^{-s\pi}} \right),$$

$$\eta_2 = w_2 \left(\frac{4s}{s^2 + 5 + F} \frac{1}{1 - e^{-s\pi}} \right). \quad (16)$$

Below, we only consider the case $F = 0$ (for which $\nu_1 = \nu_2 = \mu$) just as in section 3. The nondimensional parameter β does not enter in the coefficients of the truncated model since the term $\partial \Psi / \partial x$ is orthogonal to the basis. The Rossby dynamics are thus filtered out.

Rescaling time with λ, we rewrite (14) as

$$\dot{A} = AB - rA + \frac{\delta}{r}, \qquad \dot{B} = -A^2 - rB + r^2\gamma, \quad (17)$$

with $r = \mu/\lambda$, $\gamma = \lambda\eta_2/\mu^2$, $\delta = \mu\eta_1/\lambda^2$, and the dot refers to differentiation with respect to λt.

b. Analysis of steady states and stability

Steady states (A_0, B_0) are obtained by solving a cubic equation for A_0 and are given by

$$A_0^3 + r^2(1 - \gamma)A_0 - \delta = 0;$$

$$B_0 = r\gamma - \frac{A_0^2}{r}. \quad (18)$$

The linearization of the system (17) around a steady state (A_0, B_0) gives the Jacobian matrix

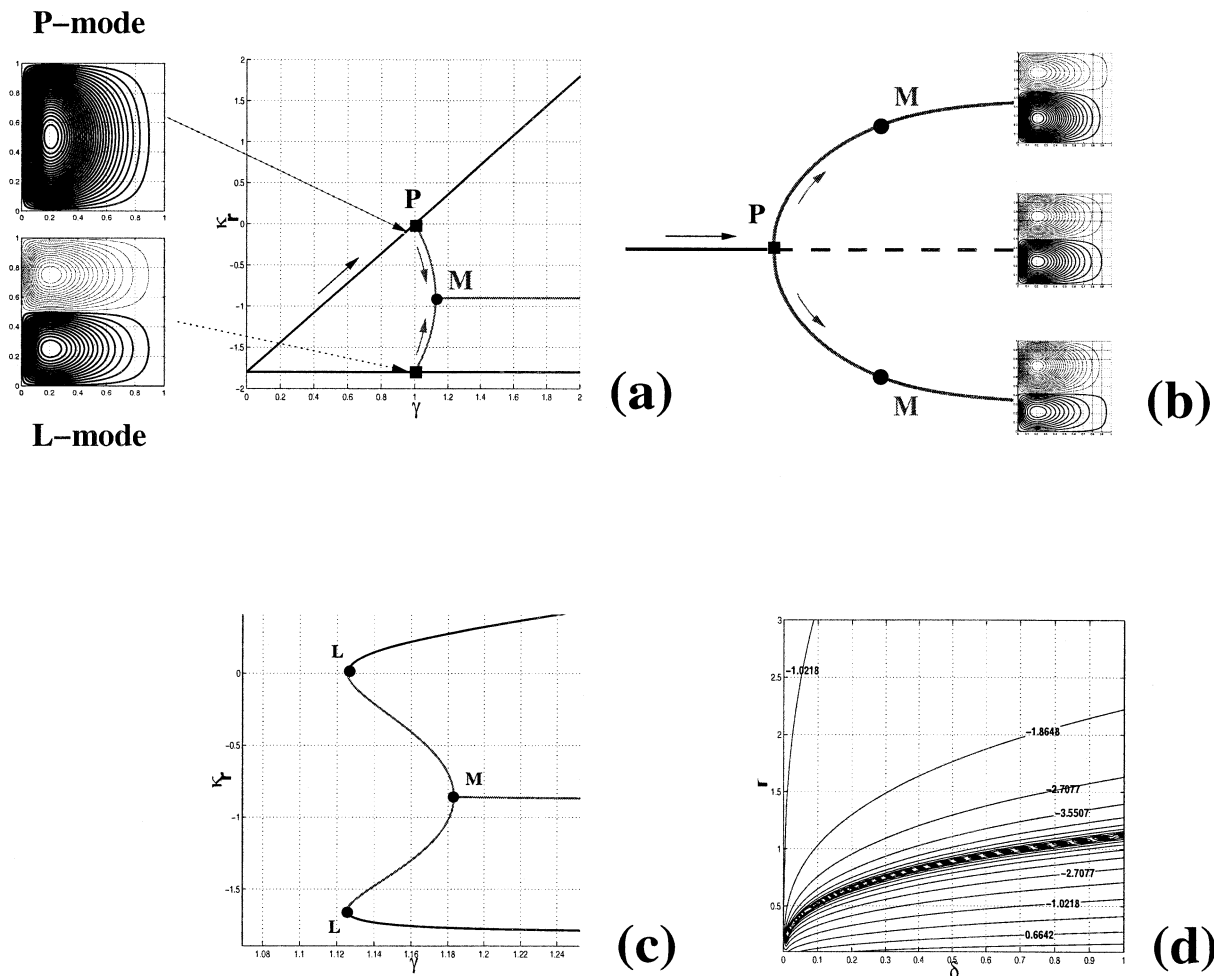$$\begin{bmatrix} B_0 - r & A_0 \\ -2A_0 & -r \end{bmatrix}, \quad (19)$$

P–mode

L–mode

FIG. 6. Spectral behavior of the low-order QG model. Path of the real part of the two eigenvalues. (a) Idealized case ($\delta = 0$, $r = 1.8$) with streamfunction anomalies. (b) Sketch of the bifurcation diagram with the basic states. (c) Corresponds to the perturbed case and for the disconnected branch ($\delta = 0.1$, $r = 1.8$). (d) The $\log_{10}$ contour lines of $\gamma_M - \gamma_{LP}$ (as explained in the text) as a function of r and δ.

The eigenvalues κ of (19) are solutions of the quadratic equation

$$(\kappa + r)^2 - B_0(\kappa + r) + 2A_0^2 = 0. \tag{20}$$

Consider first the case $\delta = 0$, for which the flow is forced by an antisymmetric wind stress curl ($\eta_1 = 0$). For $\gamma < 1$, only one steady state $(A_0, B_0) = (0, r\gamma)$ exists and is stable since the eigenvalues of (20) are $r(\gamma - 1)$ and $-r$. Both eigenvalues are plotted in Fig. 6a as a function of γ for $r = 1.8$. At $\gamma = 1$, a pitchfork bifurcation occurs leading to the coexistence of three different steady states for $\gamma > 1$. The eigenvalue $r(\gamma - 1)$ becomes positive for $\gamma > 1$ so that the antisymmetric solution $(0, r\gamma)$ is now unstable. The asymmetric solutions arising at P are $(\epsilon_b r\sqrt{\gamma - 1}, r)$ with $\epsilon_b = \pm 1$. A sketch of the bifurcation diagram is shown in Fig. 6b, showing also patterns of the asymmetric solutions, for which there is simply a meridional shift of the jet axis.

The asymmetric solutions are stable because $\kappa_r < 0$

along these branches. The analytical expression of the eigenvalues is

$$\kappa_{1,2} = \begin{cases} -\dfrac{r}{2} \pm \dfrac{r}{2}\sqrt{9 - 8\gamma} & \text{for } 1 \le \gamma \le \dfrac{9}{8} \\[3mm] -\dfrac{r}{2} \pm i\dfrac{r}{2}\sqrt{8\gamma - 9} & \text{for } \dfrac{9}{8} \le \gamma. \end{cases} \tag{21}$$

Hence, the real eigenvalues of the system (19) come together at $\gamma = \gamma_M = 9/8$ to become oscillatory with a nonzero imaginary part. The two modes involved in this process are precisely the asymmetric P-mode $(1, 0)$ responsible for the multiplicity of the solutions and the antisymmetric L-mode $(0, 1)$, which controls the intensity of the gyres. For $\gamma > \gamma_M$, the two oscillatory conjugate modes (the eigenvector Φ, corresponding to the oscillatory gyre modes) are given by

$$\Phi = \frac{1}{2\sqrt{3}} \frac{1}{\sqrt{\gamma - 1}} \left(\begin{bmatrix} 2\sqrt{\gamma - 1} \\ -1 \end{bmatrix} \pm i \begin{bmatrix} 0 \\ -\sqrt{8\gamma - 9} \end{bmatrix} \right).$$

(22)

This merging process exactly represents what happens in the barotropic QG model results in section 3. The imaginary part of the gyre mode is almost zero close to $\gamma = \gamma_M$ and has its spatial structure similar to the L-mode (0, 1). The spatial structure of the real mode is inherited from the P-mode and the merging depends on the asymmetry of the steady flow.

For a slightly asymmetric wind stress ($\delta \neq 0$), the number of steady solutions (A_0, B_0) of (18) depends on the sign of the discriminant

$$D = \delta^2 + \frac{4}{27}[r^2(1 - \gamma)]^3.$$

For $D > 0$, (18) admits one real solution

$$A_0^1 = \left[\frac{\delta + \sqrt{D}}{2} \right]^{1/3} - \frac{r^2}{3}(1 - \gamma) \left[\frac{\delta + \sqrt{D}}{2} \right]^{-1/3},$$

and for $D < 0$, that is for $\gamma > \gamma_{LP} = 1 + (3/r^2)[(\delta/2)]^{2/3} > 1$, there are three distinct solutions

$$A_0^k = -\frac{2}{\sqrt{3}}r\sqrt{\gamma - 1} \cos\frac{\alpha + 2k\pi}{3}, \qquad k = 1, 2, 3,$$

where $\alpha = \pi - \arctan(\sqrt{-D/\delta})$. This solution structure is similar to that in Fig. 5. On the isolated branch, the real part of the leading eigenvalue κ_r is plotted in Fig. 6c for $\delta = 0.1$ and $r = 1.8$. The merging of the stationary modes occurs again at the point M, very similar to that in Fig. 5c.

As a matter of fact, the P-mode and L-mode always merge in this low-order model. Figure 6d shows the difference between the value of $\gamma = \gamma_M$, when the two eigenvalues are merging, and the value of $\gamma = \gamma_{LP}$ corresponding to the appearance of the limit point L in Fig. 6c when $D = 0$. This difference depends on δ and r and it appears to be always positive. Such a behavior is an indication of the robustness of the merging between the two modes on the isolated branch. For $\delta = 0$, we find that this difference is equal to 1/8, independently of r, and consistent with (21).

c. Physical mechanism of the oscillation

The very good agreement of the merging process in both the full and the low-order QG model motivates us to investigate the physical oscillation mechanism in the low-order model for the simplest case where merging occurs ($\delta = 0$). Since the story is subtle, the investigation is divided into three parts. First, an energy equation for the perturbations on a steady flow is derived. Then follows the most difficult step, in which the tendencies of the symmetric part of the perturbation are linked to the sign of its antisymmetric part. Once this

has been established, the oscillatory mechanism can be explained.

1) ENERGY EQUATION

Let (A_0, B_0) be a steady solution of the low-order model, corresponding to $\Psi_0 = G(x)(A_0 \sin y + B_0 \sin 2y)$, with velocity field $U_0 = -\partial\Psi_0/\partial y$ and $V_0 = \partial\Psi_0/\partial x$. Consider $a = A - A_0$ and $b = B - B_0$ as the perturbations on this solution. These perturbations satisfy

$$\frac{da}{dt} + (r - B_0)a - bA_0 = ab$$

$$\frac{db}{dt} + rb + 2aA_0 = -a^2.$$ (23)

Defining the perturbation kinetic energy $e = (a^2 + b^2)/2$, we see that it is indeed proportional to the energy of the perturbation $\phi = G(x)(a \sin y + b \sin 2y)$, that is, $e = C \int \phi^2 \, dx \, dy$, where the integral is over the domain $[0, \pi] \times [0, \pi]$ and C is a positive constant. Multiplying (23) by a and b, respectively, and summing, one obtains

$$\frac{de}{dt} + 2re = a^2 B_0 - abA_0.$$ (24)

The right-hand side of (24) corresponds precisely to the energy production due to the interaction between the basic flow Ψ_0 and the perturbation ϕ; that is,

$$\frac{de}{dt} + 2re = C \int J(\phi, \Psi_0)\nabla^2\phi \, dx \, dy.$$ (25)

Note that this equation is also valid in the full QG model except that e has to be replaced by $\int |\nabla\phi|^2 \, dx \, dy$.

When the spatial pattern of the perturbations resembles the steady flow, the energy production is weak, since $J(\phi, \Psi_0) \approx 0$. The right-hand side in (24) can be written as

$$\int J(\phi, \Psi_0)\nabla^2\phi \, dx \, dy$$

$$= \int \left(v^2 \frac{\partial U_0}{\partial x} - uv \frac{\partial V_0}{\partial x} \right) dx \, dy,$$ (26)

where $u = -\partial\phi/\partial y$ and $v = \partial\phi/\partial x$ are the perturbation horizontal velocities. The Reynold stress terms involving v^2 and uv in (26) can produce energy through the horizontal shear of the basic flow.

Consider now the interaction of an antisymmetric steady solution $(0, r\gamma)$ and an antisymmetric perturbation of the form $(0, \pm b_0)$. In this case, the disturbance has exactly the same spatial structure as the basic flow and hence $J(\phi, \Psi_0) = 0$. It is not possible to extract energy from the shear in this case, the amplitude of the disturbance decreases due to friction and the steady flow is stable.

On the contrary, when the antisymmetric steady flow is subjected to a symmetric perturbation of the form
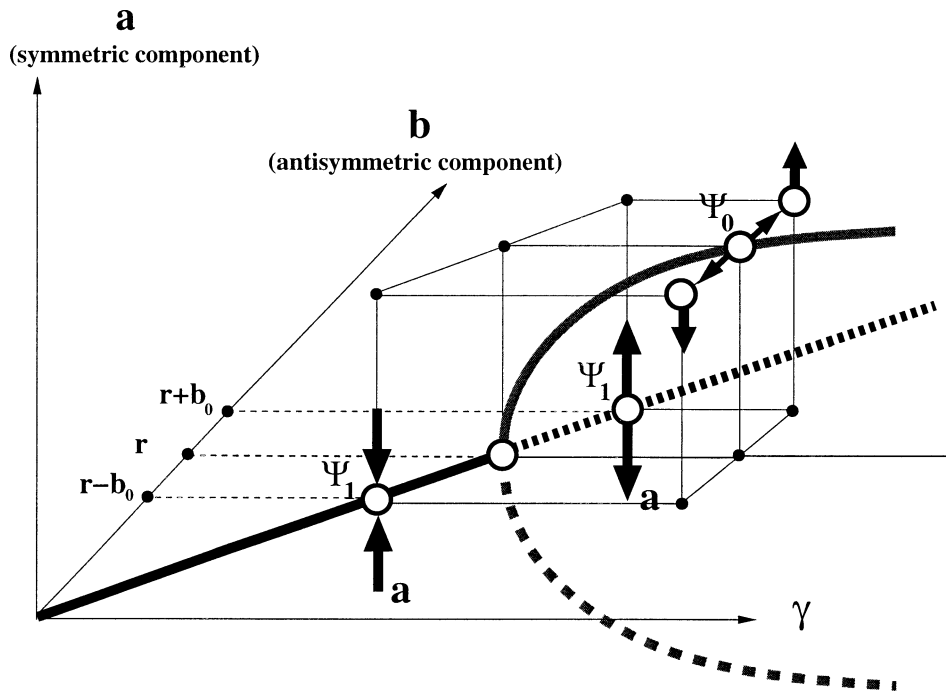
Fig. 7. Schematic drawing of the symmetry-breaking mechanism acting on an asymmetric solution Ψ_0 perturbed by an antisymmetric component $\pm b_0$. The bifurcation diagram is plotted in the three-dimensional space (γ, b, a).

$(\pm a, 0)$, it may become unstable. The first integrand $(v^2)\partial U_0/\partial x > 0$ on the rhs of (26) is the one that contributes the most to the production of energy, because the zonal velocity for such a symmetric disturbance is very weak (there is no eastward jet) and thus the term uv is small. Moreover, since the velocities of the steady flow increase with γ, the energy production is roughly proportional to γ. In the low-order model it is actually equal to $B_0 a^2 = r\gamma a^2$. When γ is large enough ($\gamma > 1$), it is able to overcome the dissipation and lead to growth of the perturbation. This mechanism gives an efficient way to reduce the energy of the antisymmetric flow (with energy $E_k = \frac{1}{2} r^2 \gamma^2$) by making the flow asymmetric (with energy $E_k = \frac{1}{2} r^2 \gamma$) and less energetic. Moreover, such a mechanism explains why a saddle–node bifurcation is less likely to occur first, since antisymmetric perturbations extract energy in a much less efficient way than do symmetric perturbations.

This analysis provides added rigor to the symmetry-breaking mechanism described by Dijkstra and Katsman (1997).

2) Temporal constraints

The symmetry-breaking mechanism introduces constraints on the tendencies of the symmetric component of the perturbations. To demonstrate this, multiply (17a) by A to derive an energy equation for the symmetric part of the flow $AG(x) \sin y$. With $e^+ = A^2/2$, one obtains

$$\frac{de^+}{dt} = 2e^+ b. \tag{27}$$

This equation shows that if one increases the antisymmetric component b of the flow such that it becomes less asymmetric, the response is to increase the symmetric component $a = A - A_0$ of the flow so that it becomes again more asymmetric. Thus the antisymmetric disturbance b cannot just change without altering the intensity of the symmetric component a of the flow.

To explain the temporal constraints implied by (27), let us focus on an asymmetric (unstable) steady-state solution $\Psi_0 \equiv (A_0, B_0) = (r\sqrt{\gamma - 1}, r)$. This solution has a larger (in size) subtropical gyre that also means a more intense one in the truncated model. Let Ψ_0 be perturbed and consider the problem (14) with initial condition at $t = 0$:

$$(A(0), B(0)) = (A_0, B_0) + (a_0(0), b_0(0)) \equiv \Psi_0 + \phi_0(0),$$

where $a_0(0)$ and $b_0(0)$ are arbitrary disturbances of Ψ_0. We can write this initial condition also as

$$(A(0), B(0)) = (A_1, B_1) + (a_1(0), b_1(0)) \equiv \Psi_1 + \phi_1(0),$$

where $\Psi_1 = (A_1, B_1) = (0, r + b_0(0))$ is a perturbed antisymmetric state and $a_1(0) = A_0 + a_0(0)$ and $b_1(0) = 0$.

The decomposition into $\Psi_1 + \phi_1$ provides an interesting interpretation and the corresponding geometric situation is sketched in Fig. 7.

With respect to the steady state Ψ_1, the energy $e_1(t)$ of the perturbation $(a_1(t), b_1(t))$ now satisfies

$$\frac{de_1}{dt} + 2re_1 = r^2\gamma_2 b_1$$

$$+ C \int \left[v_1^2 \frac{\partial U_1}{\partial x} - u_1 v_1 \frac{\partial V_1}{\partial x} \right] dx \, dy, \quad (28)$$

where U_1 and V_1 correspond to the velocities of the antisymmetric flow Ψ_1 while the wind stress forcing term in (17) is split into two parts, $r^2\gamma = r^2(\gamma_1 + \gamma_2)$. The part $r^2\gamma_1$ corresponds to the forcing needed to obtain the solution Ψ_1. The term $r^2\gamma_2 b_1 = r^2 b_1(\gamma - 1 - b_0/r)$ can readily be interpreted as the work exerted by the wind stress on the perturbation flow; that is, $r^2\gamma_2 b_1 = C \int (u_1 \tau_2^x + v_1 \tau_2^y) \, dx \, dy$. This work does not depend on the asymmetry of the flow, due to the idealized structure of the wind stress, and it is initially zero. Note also that no assumption has been made regarding the size of the perturbation in (28) because of energy conservation in the full QG model, $\int J(\nabla^2\phi, \phi)\phi \, dx \, dy = 0$.

At this point, we can use the information from the bifurcation diagram shown in Fig. 7. When $b_0 > 0$, the state Ψ_1 is located to the right of the pitchfork bifurcation ($r + b_0 > r$) and it is unstable. Since the initial amount of work $r^2\gamma_2 b_1(0)$ is zero ($b_1(0) = 0$), the symmetric perturbation $a_1 = A_0 + a_0$ must grow and hence $da_0/dt > 0$. In the case where $b_0 < 0$, the flow Ψ_1 is stable and hence $da_0/dt < 0$. The results on the temporal constraints, caused by this symmetry-breaking dynamics, can hence be summarized in the following way:

- disturbance $(\pm a_0, +b_0) \Rightarrow \dfrac{da}{dt} > 0$

- disturbance $(\pm a_0, -b_0) \Rightarrow \dfrac{da}{dt} < 0.$ (29)

The law (29) indeed determines the direction of propagation of the anomalies, which, in the truncated model case, is northward for a more intense subtropical gyre. The fact that in more realistic models the direction of propagation is reversed (i.e., southward) should not be objectionable: an antisymmetric anomaly goes in the southward direction so as to enhance the strength of the more intense subtropical gyre. In realistic models, a more intense subtropical gyre has a relative size that is smaller although it has more relative vorticity than the subpolar gyre. On the contrary, in the truncated model, a more intense subtropical gyre has also a larger relative size than the subpolar gyre. This difference explains why in realistic models the direction of propagation is reversed and is southward. In the truncated model, the anomaly with positive vorticity must grow in size in order to achieve the same goal: that is the direction of propagation must be reversed (see Fig. 8). Both cases follow precisely the universal law (29) that is dictated by the symmetry-breaking mechanism, no matter the complexity of the models studied.

3) THE OSCILLATORY MECHANISM OF THE GYRE MODE

We are now able to explain the appearance of the oscillatory mode when the asymmetry of the steady state is large enough. Consider γ very large so that the asymmetry of the basic state is accentuated. In this case, the energy production term $\int J(\phi, \Psi_0)\nabla^2\phi \, dx \, dy$ can be well approximated by $-abA_0$ [see rhs of (24)]. Assume further that the asymmetric solution $(A_0, B_0) = (r\sqrt{\gamma - 1}, r)$ is initially perturbed by $(0, b_0)$, with $b_0 > 0$. For a large value of γ, a trajectory of (17)—corresponding to one cycle of the oscillation—is plotted in the upper-right panel of Fig. 8.

If a and b are of the same sign, the shear decreases the energy of the anomaly (Fig. 8, stage 2). On the contrary, if a and b are of opposite sign, the disturbances are able to extract energy from the steady flow so that e increases (Fig. 8, stage 4).

The oscillation involved in the gyre mode can now be described as consisting of four distinct steps, as illustrated in Fig. 8.

(i) In stage 1 the antisymmetric part of the solution is positive, $b_0 > 0$, and so the symmetry-breaking mechanism increases the asymmetric component because $da/dt > 0$. The shear and the friction (which is small for large γ) act together to stabilize the solution (stage 2) and hence the energy e must decrease. Since b is positive and $da/dt > 0$, however, a cannot decrease and thus b must decrease. This continues until b crosses the zero axis, in stage 3, and becomes negative due to friction.

(ii) At stage 4 in Fig. 8, a and b are of opposite sign so that the energy of the disturbance must grow due to the shear. However, it is impossible for a to increase because b is negative and consequently $da/dt < 0$. Thus b must decrease further to more negative values.

(iii) When a crosses the zero axis, a and b are of the same sign so that a situation similar to that in (i) occurs, that is, the shear stabilizes the flow. However, $b < 0$ implies that $da/dt < 0$ and hence a becomes even more negative. Consequently, the value of b must increase to less negative values.

(iv) When b becomes positive again, the shear destabilizes the flow again, e increases while simultaneously $da/dt > 0$ so that a becomes less negative. Consequently, the value of b must increase. When a becomes zero, case (i) is obtained and the cycle starts all over again.

As a matter of fact, the loss of energy during the two phases (i) and (iii) makes the energy of the disturbance slowly decrease.
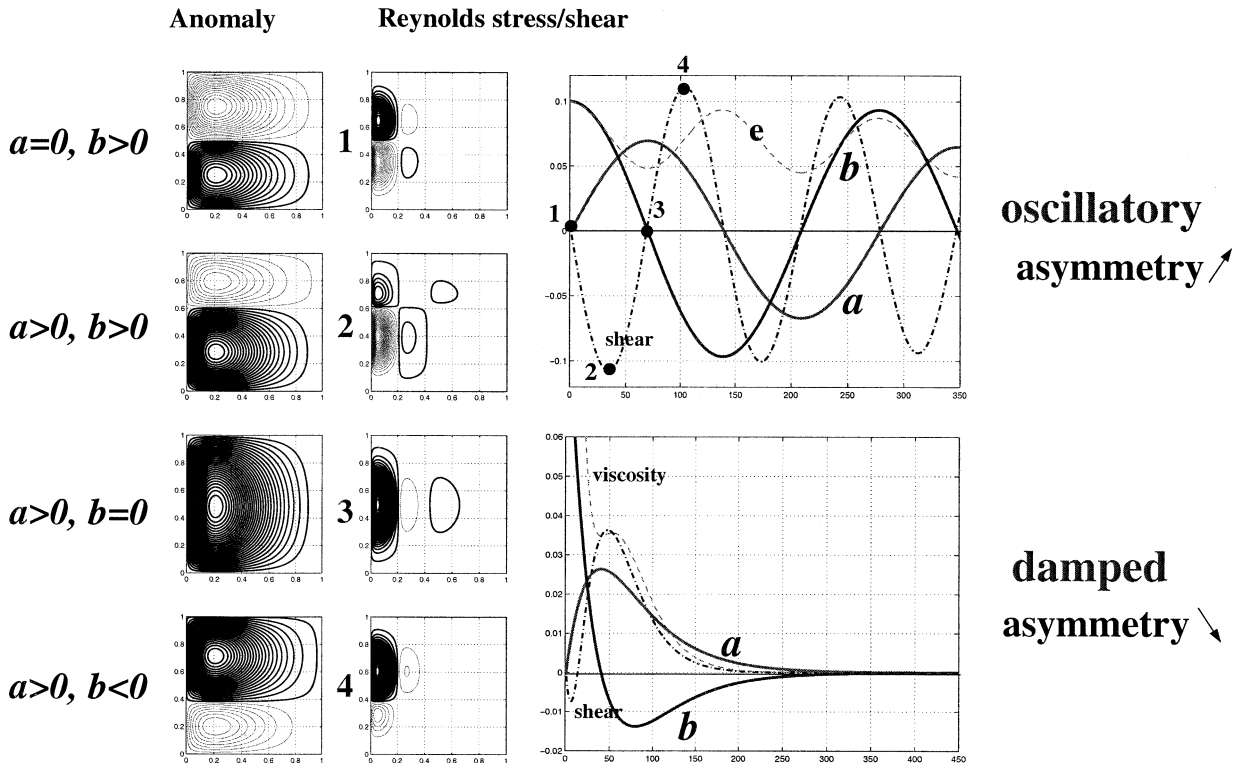
FIG. 8. Time integration of (17) for $r = 1$ and $\delta = 0$. (right panels) The behavior of $a = A - A_0$ and $b = B - B_0$. The energy of the anomalies $e = (a^2 + b^2)/2$ (amplified by a factor 10) and the shear of the flow due to Reynolds stress $\int [v^2(\partial U_0/\partial x) - uv(\partial V_0/\partial x)]\,dx\,dy$ are indicated for two cases: oscillatory (upper-right panel, $\gamma = 1025$) and damped (lower-right panel, $\gamma = 1.12$). For the damped case, the friction $2r(a^2 + b^2)/2$ is shown instead and both shear and friction have been amplified by a factor 50. (left panels) Corresponds to the anomalies ϕ and to the energy production due to the shear (oscillatory case).

The mechanism above explains why γ needs to be large enough for this oscillation to occur. As was apparent in steps (i) and (iii), the shear and friction act together to stabilize the flow (stage 2, Fig. 8). However, in steps (ii) and (iv), they act on the growth of the perturbation in an opposite way so that if the asymmetry of the flow is not strong enough to overcome the effect of the dissipation, then b may increase before a becomes zero. In that case, a decreases less and less and both a and b tend exponentially to zero with opposite sign. Indeed, this situation where the dissipation overcomes the effect of the shear, so as to damp the solution, does occur for $1 < \gamma < 9/8$. Such a situation is shown in the lower-right panel of Fig. 8.

5. Summary and discussion

The purpose of this study was to clarify the spectral origin and the physical mechanism of the so-called (oscillatory) gyre mode that is found in many models of the wind-driven ocean circulation. The gyre mode is distinguished from the other modes (Rossby basin modes, wall-trapped modes, and baroclinic modes) by its low-frequency behavior. The oscillatory behavior is characterized by a wave pattern that propagates per-

pendicularly to the direction of the jet, that is, either in a northwestward or southwestward direction.

In our barotropic QG model, this mode arises through merging of two nonoscillatory modes. We called the first one P-mode—P for *pitchfork*—and it is responsible for the appearance of multiple steady states. Its spatial structure consists of a tripole that is symmetric with respect to the midaxis of the basin (Fig. 3a). The spatial pattern of the second one, which we called the L-mode—L for *limit* point—is antisymmetric and dipolar. These two modes tend to deform along the asymmetric branches of solutions in such a way that they become identical and merge to become oscillatory: a gyre mode results from this merging (Figs. 3 and 4).

At first sight, this process may seem fortuitous and specific to the particular model but the study of a low-order QG model (Jiang et al. 1995) that has only two degrees of freedom indicates that this merging is more general. The dynamical mechanism leading to the appearance of the oscillatory gyre mode in this simple model is the same as the one in the full barotropic QG model. From the low-order model, the heart of the physics of the oscillatory gyre mode can be captured.

The growth and decay of the energy of the mode in the different stages of the oscillation is determined by

a pure shear mechanism. The combined effect of this shear, the asymmetry of the steady flow and the symmetry-breaking mechanism—which induces temporal constraints between the symmetric and antisymmetric components of the perturbations—cause the low-frequency oscillation. In this way, the oscillatory behavior of the gyre mode is linked to the same mechanisms that lead to the appearance of multiple equilibria at the (first) pitchfork bifurcation. In some sense, the oscillatory gyre mode on the asymmetric branch tries to reproduce the symmetry-breaking mechanism but can never reach a new equilibrium state because of the asymmetric structure of the background flow. Moreover, the orthogonality between the basis and the β term shows that this mechanism is free of Rossby dynamics.

Pitchfork bifurcations are structurally unstable so that a slight perturbation of the symmetry (8) leads to the occurrence of a so-called perturbed pitchfork bifurcation. This kind of phenomena occurs in particular in shallow-water models but also in QG ones when the bathymetry, the boundary conditions, or the shape of the wind stress is no longer symmetric. However, oscillatory gyre modes appear to be very robust to such perturbations and our study is relevant to more complex situations including primitive equations. Indeed these modes are as robust as the (perturbed) pitchfork bifurcation itself. In the single-gyre case, the lack of symmetry leads to the appearance of saddle–node bifurcations as found in many studies (e.g., Sheremet et al. 1997). In this case, we may conjecture that oscillatory gyre modes cannot develop. The nonoscillatory recirculation gyre mode of Sheremet et al. (1997) indeed should correspond to our so-called *L*-mode, which is responsible for saddle–node bifurcations (or limit points). These points will be clarified in a future work.

On a more abstract level, the mechanism of mode merging is related to a particular case of a codimension-2 bifurcation often referred in the literature as a Bogdanov–Takens bifurcation (Guckenheimer and Holmes 1983). This bifurcation corresponds to a situation where two real eigenvalues coalesce on the imaginary axis, that is, in the case where the merging point M and the pitchfork bifurcation coalesce. The normal form of this codimension-2 bifurcation is

$$\dot{x} = y \qquad \dot{y} = \mu_1 + \mu_2 y + x^2 + xy. \qquad (30)$$

The full solution structure as a function of the two parameters μ_1 and μ_2 is described in Guckenheimer and Holmes (1983). Hopf bifurcations occur in this case along the curve $\mu_1 = -\mu_2^2$, and low-frequency oscillations are expected since the frequency of the eigenmodes at the merging point is zero. Hence, the phenomenon of merging as described here is much more general and occurs, for example, also in a three-box model of the thermohaline circulation in a double-hemispheric configuration (Welander 1986; Thual and McWilliams 1992), where it leads to low-frequency "thermohaline loop" oscillations.

With this explanation of the gyre mode, the physics of all the classes of modes found in the double-gyre wind-driven ocean circulation is clarified. This being so, the intricate interaction of these modes, leading to the complex temporal variability found in numerical models and presumably in the ocean can be studied with greater confidence.

REFERENCES

Berloff, P. S., and J. McWilliams, 1999: Large-scale, low-frequency variability in wind-driven ocean gyres. *J. Phys. Oceanogr., 29,* 1925–1945.

Cessi, P., and G. R. Ierley, 1995: Symmetry-breaking multiple equilibria in quasi-geostrophic, wind-driven flows. *J. Phys. Oceanogr., 25,* 1196–1202.

Chang, K. I., K. Ide, M. Ghil, and C.-C. A. Lai, 2001: Transition to aperiodic variability in a wind-driven double-gyre circulation model. *J. Phys. Oceanogr., 31,* 1260–1286.

Corti, S., F. Molteni, and T. N. Palmer, 1999: Signature of recent climate change in frequencies of natural atmospheric circulation regime. *Nature, 398,* 798–802.

Dijkstra, H. A., 2000: *Nonlinear Physical Oceanography.* Kluwer Academic, 480 pp.

——, and C. A. Katsman, 1997: Temporal variability of the wind-driven quasi-geostrophic double gyre ocean circulation: Basic bifurcation diagrams. *Geophys. Astrophys. Fluid Dyn., 85,* 195–232.

——, and M. J. Molemaker, 1999: Imperfections of the North-Atlantic wind-driven ocean circulation: Continental geometry and asymmetric windstress. *J. Mar. Res., 57,* 1–28.

Doedel, E., and L. S. Tuckermann, 2000: *Numerical Methods for Bifurcation Problems and Large-Scale Dynamical Systems.* Springer, 119 pp.

Ghil, M., Y. Feliks, and L. Sushama, 2002: Baroclinic and barotropic aspects of the wind-driven double-gyre circulation. *Physica D,* in press.

Golubitsky, M., and D. G. Schaeffer, 1985: *Singularities and Groups in Bifurcation Theory, Part I.* Springer-Verlag, 459 pp.

Guckenheimer, J., and P. Holmes, 1983: *Nonlinear Oscillations, Dynamical Systems and Bifurcations of Vector Fields.* Springer-Verlag, 453 pp.

Ierley, G. R., and W. R. Young, 1991: Viscous instabilities in the western boundary layer. *J. Phys. Oceanogr., 21,* 1323–1332.

Jiang, S., F. F. Jin, and M. Ghil, 1993: The nonlinear behavior of western boundary currents in a wind-driven, double-gyre, shallow-water model. Preprints, *Ninth Conf. on Atmospheric and Oceanic Waves and Stability,* San Antonio, TX, Amer. Meteor. Soc., 64–67.

——, ——, and ——, 1995: Multiple equilibria, periodic, and aperiodic solutions in a wind-driven, double-gyre, shallow-water model. *J. Phys. Oceanogr., 25,* 764–786.

Keller, H. B., 1977: Numerical solution of bifurcation and nonlinear eigenvalue problems. *Applications of Bifurcation Theory,* P. H. Rabinowitz, Ed., Academic Press, 359–384.

Kubiček, M., and M. Marek, 1983: *Computational Methods in Bifurcation Theory and Dissipative Structures.* Springer-Verlag, 243 pp.

Legras, B., and M. Ghil, 1985: Persistent anomalies, blocking and

variations in atmospheric predictability. *J. Atmos. Sci.,* **42,** 433–471.

McCalpin, J., and D. Haidvogel, 1996: Phenomenology of the low-frequency variability in a reduced-gravity, quasi-geostrophic double-gyre model. *J. Phys. Oceanogr.,* **26,** 739–752.

Meacham, S. P., 2000: Low-frequency variability in the wind-driven circulation. *J. Phys. Oceanogr.,* **30,** 269–293.

Mo, K., and M. Ghil, 1988: Cluster analysis of multiple planetary flow regimes. *J. Geophys. Res.,* **93D,** 10 927–10 952.

Nauw, J. J., and H. A. Dijkstra, 2001: The origin of low-frequency variability of double-gyre wind-driven flows. *J. Mar. Res.,* **59,** 567–597.

Pedlosky, J., 1987: *Geophysical Fluid Dynamics.* 2d ed. Springer-Verlag, 710 pp.

Plaut, G., and E. Simonnet, 2001: Large scale circulation classification, weather regimes, and local climate over France, the Alps, and Western Europe. *Climate Res.,* **17,** 303–324.

Primeau, F. W. 1998: Multiple equilibria of a double-gyre ocean model with super-slip boundary conditions. *J. Phys. Oceanogr.,* **28,** 2130–2147.

——, 2001: Multiple equilibria and low-frequency variability of the wind-driven ocean circulation. *J. Phys. Oceanogr.,* in press.

Schmeits, M., and H. A. Dijkstra, 2000: Physics of the 9-month variability in the Gulf Stream region: Combining data and dynamical systems analyses. *J. Phys. Oceanogr.,* **30,** 1967–1987.

——, and ——, 2001: Bimodal behavior of the Kuroshio and the Gulf Stream. *J. Phys. Oceanogr.,* **31,** 3435–3456.

Sheremet, V. A., G. R. Ierley, and V. M. Kamenkovich, 1997: Eigenanalysis of the two-dimensional wind-driven ocean circulation problem. *J. Mar. Res.,* **55,** 57–92.

Simonnet, E., 1998: Some numerical problems related to geophysical flows. Ph.D. thesis, Université de Paris-Orsay, 154 pp.

Spall, M. A., 1996: Dynamics of the Gulf Stream/Deep Western Boundary Current Crossover. Part II: Low-frequency internal oscillations. *J. Phys. Oceanogr.,* **26,** 2169–2182.

Speich, S., H. A. Dijkstra, and M. Ghil, 1995: Successive bifurcations in a shallow-water model applied to the wind-driven ocean circulation. *Nonlin. Proc. Geophys.,* **2,** 241–268.

Stewart, W. J., and A. Jennings, 1981: A simultaneous iteration algorithm for real matrices. *ACM Trans. Math. Software,* **7,** 184–198.

Thual, O., and J. C. McWilliams, 1992: The catastrophe structure of thermohaline convection in a two-dimensional fluid model and a comparison with low-order box models. *Geophys. Astrophys. Fluid Dyn.,* **64,** 67–95.

Veronis, G., 1963: An analysis of wind-driven ocean circulation with a limited number of Fourier components. *J. Atmos. Sci.,* **20,** 577–593.

Welander, P., 1986: Thermohaline effects in the ocean circulation and related simple models. *Large Scale Transport Processes in Oceans and Atmosphere,* J. Willebrand and D. L. T. Anderson, Eds., D. Reidel, 163–200.